Geometric Properties of Nanostructured Solid Oxide Fuel Cell Electrodes

Yanxiang Zhang, Qiong Sun, Changrong Xia and Meng Ni

J. Electrochem. Soc. 2013, Volume 160, Issue 3, Pages F278-F289.
doi: 10.1149/2.057303jes

Journal of The Electrochemical Society, **160** (3) F278-F289 (2013)
0013-4651/2013/160(3)/F278/12/$31.00 © The Electrochemical Society

Geometric Properties of Nanostructured Solid Oxide Fuel Cell Electrodes

Yanxiang Zhang,[a,b] Qiong Sun,[b] Changrong Xia,[a] and Meng Ni[b,*,z]

[a] *CAS Key Laboratory of Materials for Energy Conversion, Department of Materials Science and Engineering, University of Science and Technology of China, Hefei, 230026 Anhui, China*
[b] *Building Energy Research Group, Department of Building and Real Estate, The Hong Kong Polytechnic University, Hung Hom, Kowloon, Hong Kong, China*

3D microstructures for nanostructured solid oxide fuel cell (SOFC) electrodes fabricated by infiltration/impregnation method are constructed numerically, by using a phenomenological procedure. Key geometric properties of the constructed electrodes are calculated at various infiltration loadings, including the percolation probabilities of pores and infiltrated nanoparticles, the total and active three-phase boundary (TPB) length, backbone and nanoparticles surface areas, and backbone-nanoparticles boundary area. The effects of backbone particle size, backbone porosity, nanoparticle size, and its aggregation risk are studied systematically. Analytical models are developed to predict these geometric properties, and agree well with the numerical infiltration results, as well as the literature data. It is found that the peak TPB length can be achieved at 63% coverage of the backbone surface by infiltrated nanoparticles. More interestingly, the backbone structure has little effect on nanoparticles surface area, but significantly affects TPB length, suggesting an strategy to identify electrode reaction mechanisms. Decreasing infiltrated particle size increases its surface area, enhances the peak TPB length, and decreases the optimal infiltration loading, indicating small infiltrated particles essentially benefits electrode performance. The results provide valuable information for understanding the geometric properties of the infiltrated SOFC electrodes and contribute to the design of high performance SOFC electrodes.
 [DOI: 10.1149/2.057303jes]

Manuscript submitted December 4, 2012; revised manuscript received January 3, 2013. Published January 19, 2013.

In the last decade, infiltration/impregnation technique has drawn tremendous attention in the community of solid oxide fuel cells (SOFCs) to prepare nanostructured high performance SOFC electrodes. The performance of infiltrated electrode is much higher than conventional electrodes prepared by mixing and sintering processes.[1] Theoretical and experimental studies[2–5] suggest that the promotion in electrode performance derives from the advanced microstructures by its distinctive fabrication processes. In general, the infiltration approach involves making a porous backbone layer of electrolyte material onto the dense electrolyte layer by printing/casting and co-sintering processes, then infiltrating the electrocatalyst nitrate solution into the backbone pores, followed by relatively low temperature calcinations.[6] The multiple steps permit the separate control and optimization of the backbone and the electrocatalyst structures. The low calcination temperature can suppress the detrimental reactions between the electrolyte and electrocatalyst/electrode materials.[7] More importantly, nanosized electrocatalytic particles can be formed in typical range of 50 $\sim$ 100 nm.[1] This unique structure results in a significant enhancement in electrochemical active sites for electrode reactions.

From the phenomenological standpoint, the electrode performance is directly linked with the electrode geometric properties. One of the most important geometric properties is the three-phase boundary (TPB) line, where the ionic conducting phase (backbone phase), electronic conducting phase (electrocatalyst phase), and the pores meet with each other. Many works show that the electrode performance is directly linked with the TPB length.[8] This is particularly true for the (La,Sr)MnO_3 (LSM) – yttria-stabilized zirconia (YSZ) composite electrodes,[9] because LSM (YSZ) is almost a pure electronic (oxygen ionic) conductor, and thus the electrode reactions are restricted to the TPB lines with a width of atomic dimensions. Zhu et al.[2] proposed a geometric model and found orders of magnitude enhancement in TPB length of infiltrated electrodes, compared with the conventional composite electrodes. The model considered the conventional composite electrode as a random packing system of LSM and YSZ spherical particles, and modeled the infiltrated electrode as a sphere-packed backbone, entirely coated with single-layer nanoparticles of another phase. By incorporating the charge-transfer resistance per TPB length and the ionic conductivity of YSZ, the particle-layer model[10] confirmed that: (1) the area specific resistance (ASR, Ωcm^2) of the LSM infiltrated YSZ electrodes can be much smaller than that of the conventional LSM-YSZ electrodes; and (2) the ASR value is inversely proportional to the square root of volumetric TPB length. However, this conclusion may not be applicable to all electrode materials. When the mixed-conducting perovskite, such as (La,Sr)(Co,Fe)O_3 (LSCF), or (La,Sr)FeO_3 (LSF) is used as the infiltration phase for cathodes, oxygen ions can transport through the perovskite bulk. As a result, the area for oxygen adsorption and incorporation is extended from the contacting lines (TPB) to the surface of the infiltrated nanoparticles. Moreover, the charge-transfer area is broadened to the interface of backbone-nanoparticles boundaries.[8] Based on experiments, Shah et al.[4] developed a surface resistance (SR) model for infiltrated SOFC electrodes. They found that that the ASR of LSCF infiltrated $Ce_{0.9}Gd_{0.1}O_{1.95}$ (GDC) electrodes depends on the fundamental ASR of LSCF surface, and the electrode ASR (600°C) is inversely proportional to the LSCF nanoparticles surface area. More recently, Rainer and Gorte[11] showed that the ASR (600°C) of LSF infiltrated YSZ electrodes depends strongly on the LSF surface area but is independent of LSF film thickness. These studies suggest that the surface area of infiltrated mixing-conducting phase is a key parameter for the electrode performance. Partially because of this, the infiltrated mixing-conducting phase is usually idealized as a dense thin film coating on the surface of backbone structure (indicating no TPBs), which is modeled as micrometer-scale columns (or with nano-scale branches)[5] Interestingly, this configuration was used in a theoretical model (TFV model) for conventional composite SOFC electrodes by Tanner, Fang, and Virkar,[12] before the application of infiltration method in the SOFC field. Since then, the TFV model has been widely used for simulating the infiltrated electrodes. Based on TFV model, Nicholas et al.[13] modeled the infiltrated electrode structure as micrometer-scale columns coated with hemispherical nanoparticles, proposed the simple infiltrated microstructure polarization loss estimation (SIMPLE) model, and applied the SIMPLE model to predict the ASR of (Sm,Sr)CoO_3 infiltrated GDC electrodes and LSCF infiltrated GDC electrodes. These experimental studies and models (the random-packing approaches and the thin-film approaches) successfully illustrate and confirm the importance of electrode microstructures. However, the detailed geometric properties and their variations with infiltration loading and percolation behaviors still remain unclear. An in-depth understanding of the geometric properties of infiltrated electrodes is crucial to identify reaction mechanisms and to optimize the microstructure for performance enhancement.

*Electrochemical Society Active Member.
zE-mail: bsmengni@polyu.edu.hk

Three-dimensional (3D) quantification of the electrode microstructure is necessary to clarify these geometric properties. By using focused ion beam – scanning electron microscopy (FIB-SEM) or X-ray microscopy techniques, a significant progress has been made for the 3D microstructure reconstruction of conventional composite electrodes.[14,15] However, these methods are presently unable to reconstruct the infiltrated microstructures as the relative low resolutions (e.g. 10–50 nm) of these techniques are insufficient to provide microstructural information of the infiltrated nanoparticles (can be about 25 nm in radius). Apart from experimental techniques, numerical modeling offers an efficient and economical way of exploring the microstructures of SOFC electrodes. A plenty of numerical models has been developed to construct the conventional composite electrodes.[16,17] However, according to the authors' best knowledge, no numerical model has been developed for reconstructing the microstructures of SOFC electrodes with infiltrated structure.

In this work, a numerical method is first developed to construct the 3D microstructure of infiltrated SOFC electrodes. Based on the constructed microstructure, the percolation properties of infiltrated nanoparticles and pores, and the geometric properties, including TPB length, nanoparticles surface area, backbone surface area and interfacial area of backbone-nanoparticles boundaries are calculated. The effects of particle size and porosity of the backbone, and the infiltrated particle size and its aggregation risk are studied systematically. In addition, two analytical models are developed to predict these geometric properties, and are fully validated by the numerical infiltration results.

Numerical Infiltration Methodology

In practice, the infiltration procedure involves multiple steps. The backbone structure and infiltration phase are prepared at different stages, and undergo two distinctive sintering processes.[7] Ideally, the processing details should be incorporated into the modeling approach as the electrode microstructure heavily depends on the processing history. However, it is difficult to capture all these kinetic details, such as the high temperature sintering of backbone structure and the relative low temperature calcinations of infiltration inks, due to the unclear mechanisms. In this study, the numerical construction methods for the conventional composite electrodes[17] is adopted and revised to construct the infiltrated electrodes from a phenomenological standpoint. Accordingly, the infiltrated electrodes can be numerically realized by two steps – the backbone generation and the addition of infiltration phase, during which numerical sintering is included. Based on the experimental observations,[1] the backbone and infiltration phase are considered as spherical particles. Thus the numerical sintering can be simulated by allowing contact angles between particles. In the following sections, the algorithm for backbone generation and nanoparticles infiltration are described.

Backbone generation.— The backbone structure is generated by randomly dropping spherical particles within a domain with sufficient dimensions, followed by the enlargement of particles (thus allowing contact angles) to simulate sintering. This methodology is oft-used to those construction methods for conventional composite electrodes fabricated by screen printing or spin coating.[17] The domain is discretized into cubic pixels (or voxels). All the pixels of the domain are assigned a gray value of 0 to represent an empty container. Then the backbone particles are randomly packed using the morphological dilation method to form point-to-point contact, proposed in our previous study.[18] During the packing of backbone particles, the bottom and lateral boundaries act as solid walls and the top boundary is open for particles dropping into the domain. Although the particles are dropped from the top boundary, the generated backbone structures are isotropous. The particle radius is $r_{BB}\cos\theta$. The random packing procedure is repeated till the domain cannot contain any additional backbone particle. Then, the backbone particles are in situ expanded to a radius of r_{BB}, so as to create a contact angle, θ between backbone particles. Typically, θ is usually considered as 15°.[19] All the pixels belonging to the backbone particles are assigned a gray value of −1. To ensure sufficient porosity of the infiltrated electrodes, high porosity of the backbone structure is required, i.e. 40%–60%. In the fabrication procedure, usually various types of pore formers are used to control the backbone porosity. In this study, the backbone porosity is controlled by randomly erasing a certain amount of particles before enlargement.

For electrode microstructure construction, the domain size and resolution (pixel size) are very important parameters. According to the work by Cai et al.,[20] the domain side length should be at least 2.5 times particle diameter to eliminate the randomness of structure generation, and the particle diameter should be 10 times the resolution to ensure the calculation accuracy. In this study, the backbone particle diameter is selected as 0.4 μm, 0.3 μm, and 0.2 μm. Thus the domain size is set up as 1 μm × 1 μm × 1 μm. And the nanoparticle radius, r_{NP} is in range of 25 nm and 75 nm. Accordingly the resolution is 5 nm. Therefore, the domain contains 8 million pixels, requiring full performance of a 4 GB RAM computer. For the case $r_{BB} = 0.2$ μm, $r_{NP} = 25$ nm, and 10 vol.% infiltration loading, typical numbers of backbone particles and infiltrated nanoparticles are 25 and 5341, respectively. The domain size and resolution will be verified to be sufficient in the section of results and discussion.

Nanoparticles infiltration.— Nanoparticles are coated randomly onto the surface of the generated backbone structure one-by-one. Particular attention is given to the sintering and the aggregation risk of nanoparticles. The sintering of nanoparticles forms the contact angles of nanoparticle - backbone particle pair and nanoparticle - nanoparticle pair. Strong evidence for the contact angle of nanoparticle - backbone particle pair has been given by SEM micrographs. For example, Shah et al.[4] first reported that the infiltrated LSCF nanoparticles on the GDC backbone surface are hemispheres. Recently, Nicholas et al.[13] reported that the infiltrated $Sm_{0.5}Sr_{0.5}CoO_{3-\delta}$ nanoparticles on the GDC backbone surface were also hemispherical. Fig. 1 shows some typical infiltrated electrode microstructures, including LSM infiltrated YSZ electrode[21] (Fig. 1a), Ni infiltrated magnesium – doped lanthanum gallate (LSGM) electrode[22] (Fig. 1b), and Pd infiltrated YSZ electrode[23] (Fig. 1c). It can be seen that the nanoparticles in the infiltrated electrodes can be considered as hemispheres, independent of backbone morphology, nanoparticle size, and its aggregation risk. Therefore, we assume the contact angle of nanoparticle - backbone particle pair to be 90°. Fig. 1d shows the high resolution TEM for Pd infiltrated YSZ electrode.[23] It can be seen that the contact angle between Pd particles is about 60°, which is used as the contact angle between nanoparticles in this work. Accordingly, the sintering of nanoparticles is simulated by directly coating the nanoparticle with a designed radius of r_{NP} onto the backbone surface or onto the nanoparticles surface, with the nanoparticle center on the coated surface, as shown in Fig. 2. The pixel value of nanoparticles is assigned to be 1, leaving the pixel value of intersecting part with the backbone unchanged.

In practice, the aggregation is a constant obstacle to obtain uniform infiltration morphology.[1] Thus various types of infiltration inks are used, such as the aqueous of nitrate salts, and the molten nitrate salts.[7] During the infiltration procedure, if the nanoparticles prefer to be coated onto the backbone surface, the coating morphology tends to be uniform, otherwise, the nanoparticles tends to form aggregations. Obviously, this preference depends on the physical/chemical properties of the infiltration inks. In the numerical infiltration, the risk of aggregation formation (nanoparticles' preference) is represented by a weighting factor w. Before the coating of each nanoparticle, a probability is assigned for coating onto the backbone surface,

$$P_{BBS} = wArea_{BBS}/[wArea_{BBS} + (1-w)Area_{NPS}] \quad [1]$$

where w is the weighting parameter, in the range of 0 to 1. $Area_{BBS}$ [$\mu m^2 \mu m^{-3}$] is the backbone surface area after infiltration, $Area_{NPS}$ [$\mu m^2 \mu m^{-3}$] is the nanoparticles surface area as shown in Fig. 2. Thus the probability of coating on the nanoparticles surface is,

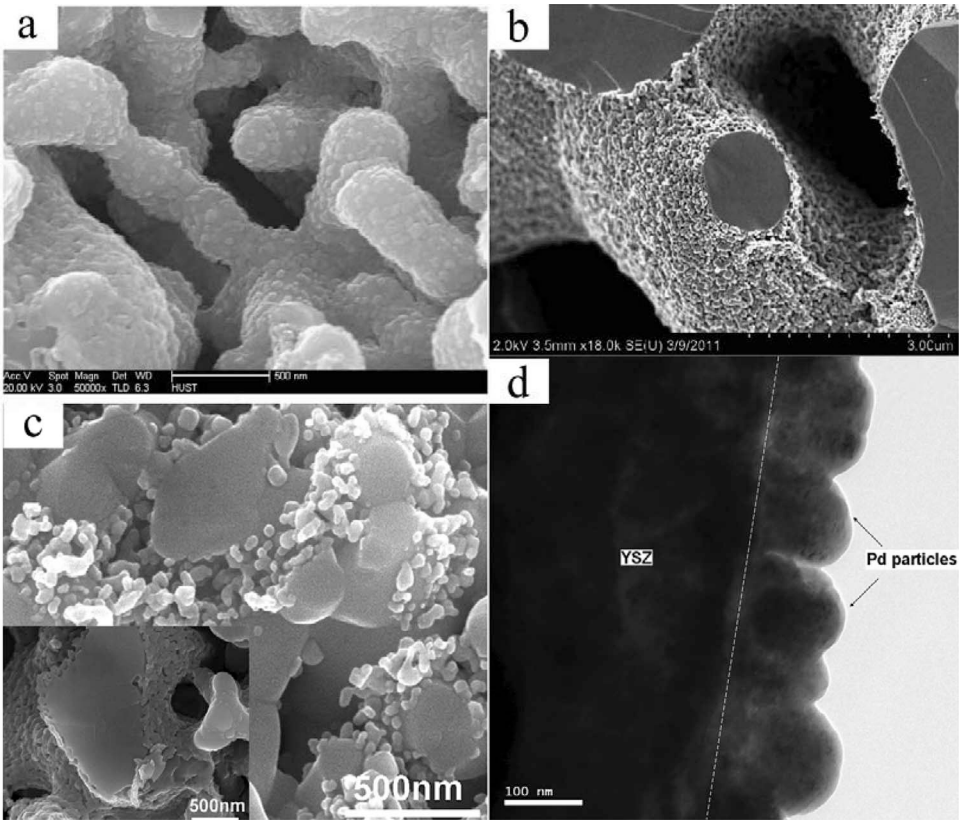

Figure 1. SEM micrographs of (a) LSM infiltrated YSZ electrode,[21] (b) Ni infiltrated LSGM electrode,[22] (c) chemically reduced and (inset of c) thermally decomposed Pd infiltrated YSZ electrode, and (d) high resolution TEM of the inset of (c).[23] (Reprinted with permission from Refs. 21–23. Copyright 2009 Elsevier for,[21] 2011 The Royal Society of Chemistry for,[22] and 2011 Elsevier for.[23]).

$P_{NPS} = 1 - P_{BBS}$. The calculation of $Area_{BBS}$ and $Area_{NPS}$ will be presented in the following section. The weighting parameter, w, will be studied to discuss its effects on aggregation risk. As indicated by Eq. 1, in case of $w = 0.5$, there is no preference of coating. If w tends to be 1, the nanoparticle prefers to be coated on the backbone surface, indicating a low aggregation risk. Thus the w has a clear physical meaning and it is linked with the properties of the infiltration inks, although this linkage is not further studied at the present stage. We conjecture w value relates with the nucleation rates of nanoparticles on the backbone surface and the nanoparticles surface.

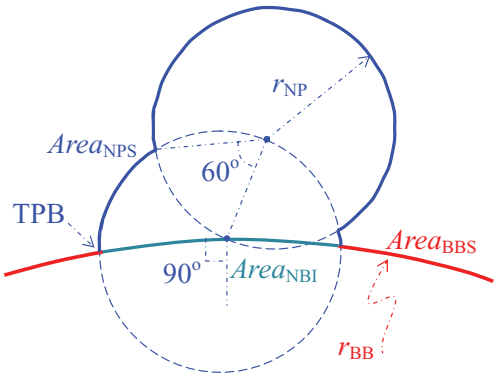

Figure 2. Illustration of nanoparticles configuration (blue) on backbone surface (red), and the definition of nanoparticles surface area, $Area_{NPS}$, backbone surface area, $Area_{BBS}$, interface area of backbone-nanoparticles boundaries, $Area_{NBI}$, three-phase boundary, TPB, and contact angles between particles. Dashed lines indicate fictional spheres, which do not exist in real microstructure.

Calculation of Geometric Properties

Fig. 2 outlines part of these geometric properties, including the nanoparticles surface area, $Area_{NPS}$ [$\mu m^2 \mu m^{-3}$], the backbone surface area, $Area_{BBS}$ [$\mu m^2 \mu m^{-3}$], the interfacial area of backbone-nanoparticles boundaries, $Area_{NBI}$ [$\mu m^2 \mu m^{-3}$], and the TPB length, $TPBL$ [$\mu m \mu m^{-3}$]. In addition, the percolation probabilities of infiltrated nanoparticles, $P_{infiltration}$, and pores, P_{pore}, as well as the percolated values of $Area_{NPS}$, $Area_{BBS}$, $Area_{NBI}$, and $TPBL$ are calculated at various infiltration loadings. The calculation method strictly follows their definitions in the discretized domain. The infiltration loading is represented by the percentage of nanoparticle pixels in the entire domain, including pores. The percolation probability of infiltrated nanoparticles/pores is defined as the total number of those nanoparticles/pores pixels connecting with the bottom and top boundaries of the domain, divided by the total amount of nanoparticles/pores pixels. A morphological labeling method with 18-connectivity is used to distinguish these percolated pixels.[24] The (percolated) $Area_{NPS}$ is defined as the total area of pixel facets belonging to (percolated) nanoparticle pixels and (percolated) pore pixels, divided by the domain volume. Similarly, the (percolated) $Area_{BBS}$ is the total area of pixel facets belonging to backbone pixels and (percolated) pore pixels, divided by the domain volume. The (percolated) $Area_{NBI}$ is the total area of pixel facets belonging to the backbone pixels and (percolated) nanoparticle pixels, divided by the domain volume. Note that these area properties are overestimated by their definitions in the discretized domain. For example, the surface area of a particle with a radius of r_{NP} is estimated as $6\pi r_{NP}^2$, higher than the theoretical value, $4\pi r_{NP}^2$. Thus these area properties are then weighted by a factor of 2/3 to eliminate this error. The (percolated) TPBL is the total length of pixel edges belonging to the backbone pixels, (percolated) nanoparticle pixels, and (percolated) pore pixels, divided by the domain volume, and a correction factor of 1.455 is used to eliminate the zigzag effect.[25]

Results and Discussion

The numerical infiltration is repeated at least two times for each condition. The discrepancy of calculation results for the same condition is found to be negligible. Fig. 3 shows the results of 5 times simulations for an infiltrated electrode with the backbone porosity of 50 vol.%, the backbone particle radius of 0.2 μm, the nanoparticle radius of 25 nm, and the weighting parameter of 0.9, approaching the oft-studied infiltrated electrodes.[4,20] As is shown, the present domain size (1 μm × 1 μm ×1 μm) and resolution (5 nm) are sufficient to study the geometric properties as well as the percolation properties. Thereafter, we select this case as the baseline condition to conduct parametrical studies.

Fig. 4 shows the 3D microstructures of infiltrated SOFC electrodes under the baseline condition with infiltration loadings of 5, 10, and 15 vol.%, corresponding to electrode porosities of 45, 40, and 35 vol.%, respectively. As shown in Fig. 3, this infiltration loading of 10 vol.% corresponds to a maximum $TPBL_{total}$. For the 10 vol.% loading, more than 99% nanoparticles are percolated and almost all the pores are percolated (Fig. 5a). In addition, the nanoparticles surface area is found to be 10 $\mu m^2 \mu m^{-3}$ (Fig. 5c), higher than the backbone surface area before infiltration, 6.8 $\mu m^2 \mu m^{-3}$ (Fig. S1). According to the definition of infiltration loading in the present study, a threshold loading of 6 vol.% of entire volume corresponds to 10.7 vol.% of solid volume, which is still much lower than the normal threshold (for percolation purpose) loading of 30 vol.% for the conventional composite electrodes, in consistent with the experimental observations.[22,26] In other words, a remarkable conductivity of infiltration phase can be obtained at relative low infiltration loadings. Since the conventional infiltration inks usually produces a limited amount of infiltration phase (i.e. 3 vol.%[7]), multiple infiltrations are required. It is expected that the geometric properties are influenced by the infiltration loading, the backbone particle size, the backbone porosity, the nanoparticle size, as well as the weighting parameter, which will be studied in the following parts.

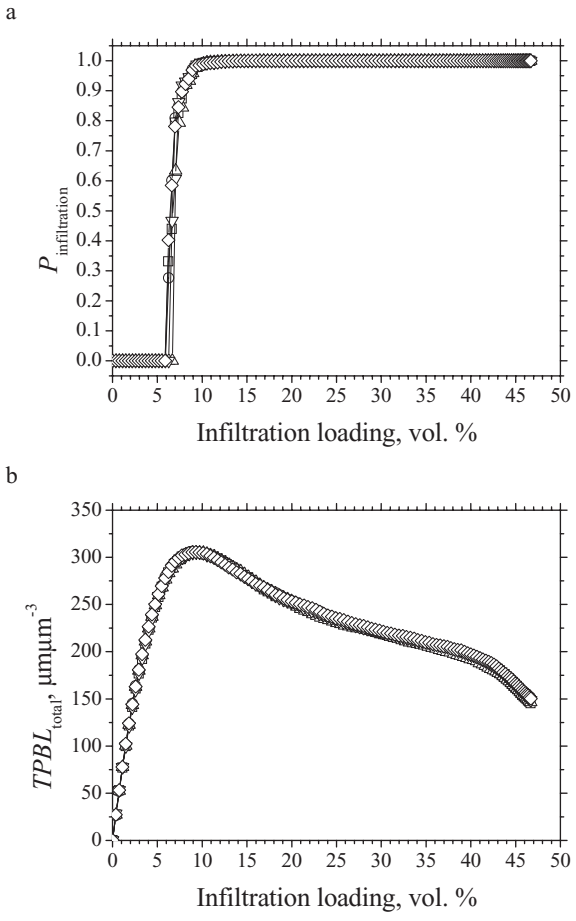

Figure 3. Sufficiency validation of the 1 μm × 1 μm × 1 μm domain size and the 5-nm resolution, by 5-times numerical infiltration results under the baseline condition (r_{BB} = 0.2 μm, backbone porosity = 50 vol.%, r_{NP} = 25 nm, w = 0.9). (a) percolation probability of nanoparticles, and (b) total TPB length.

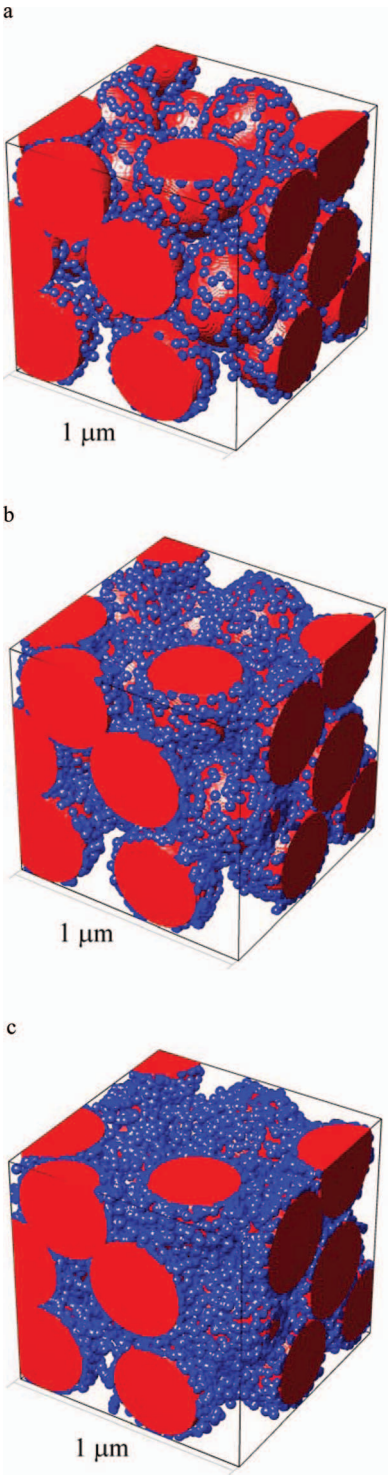

Figure 4. 3D visualization of the baseline structure with infiltration loadings of 5, 10, and 15 vol.% (r_{BB} = 0.2 μm, backbone porosity = 50 vol.%, r_{NP} = 25 nm, w = 0.9).

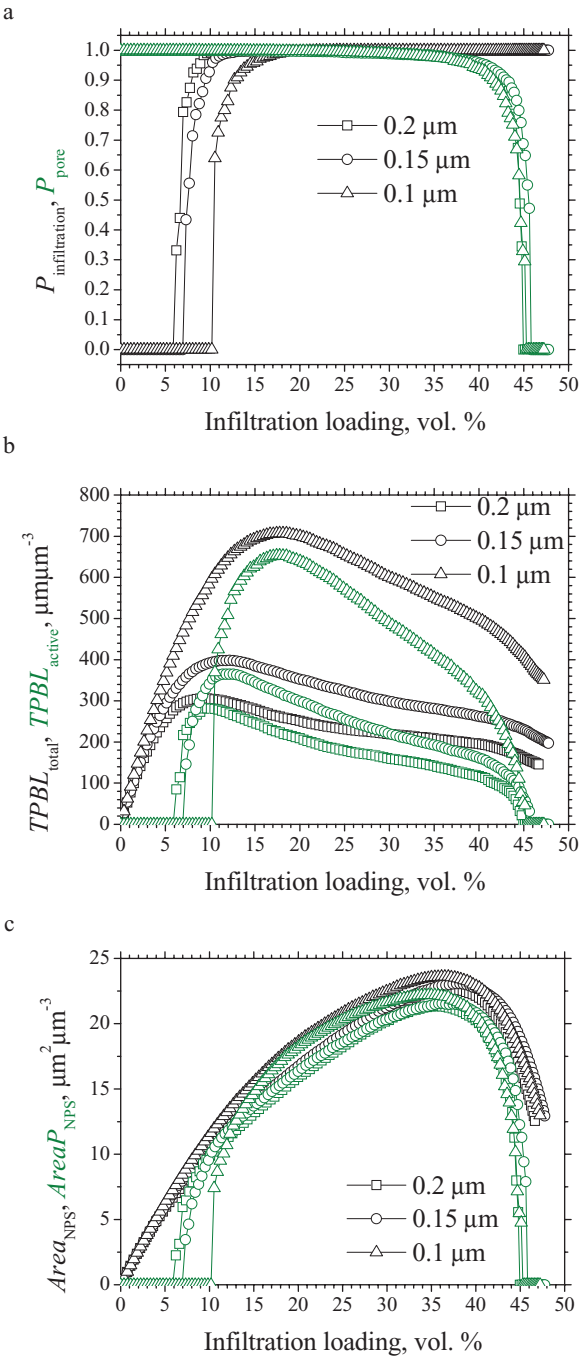

Figure 5. Calculation results of percolation probabilities of nanoparticles and pores (a), total and percolated TPB lengths (b), total and percolated nanoparticles surface areas (c) as a function of infiltration loading under various backbone particle radiuses of 0.1 μm, 0.15 μm, and 0.2 μm (backbone porosity = 50 vol.%, r_{NP} = 25 nm, w = 0.9).

Effects of backbone particle size.— In addition to the baseline condition, another two conditions with backbone particle radiuses of 0.15 μm and 0.1 μm are studied, leaving other factors unchanged, including backbone porosity, nanoparticle size, and weighting parameter. Fig. 5a shows the percolation probabilities of nanoparticles and pores as a function of infiltration loading. It is found that both the nanoparticles and pores show clear percolation thresholds with sharp transition in percolation behaviors at the thresholds. As shown in Fig. 5a, decreasing backbone particle radius increases the percolation threshold of nanoparticles. For example, the threshold loading is increased from 6 vol.% to 11 vol.%, when the backbone particle radius is decreased from 0.2 μm to 0.1 μm. The combination effects with infiltrated nanoparticle size will be discussed in Section 4.3. For comparison, the pore percolation behaviors are insensitive to the backbone particle size. In addition, more than 95% pores are percolated when the electrode porosity is higher than 10 vol.%. For example, all the pores are available for gas transport at 20 vol.% porosity.

Fig. 5b shows the evolutions of the total and active TPB length. It is found that the total TPB length initially increases with increasing infiltration loading, reaches a maximum value, and then decreases with a further increase in infiltration loading due to the contact between nanoparticles as illustrated in Fig. 1d. This tendency is clearly visualized in Fig. 4. For the low infiltration loading shown in Fig. 4a, TPB length is limited by the amount of nanoparticles. When the infiltration loading is increased (Fig. 4b), TPB length is enhanced. However, a too high infiltration loading decreases the exposed backbone surface area (Fig. 4c) and nanoparticles may not access the backbone surface, leading to a decrease in TPB length. In addition, the total TPB length highly depends on the backbone particle size. For instance, the peak $TPBL_{total}$ is enhanced from 300 μm.μm^{-3} to 700 μm.μm^{-3} when the backbone particle radius is decreased from 0.2 μm to 0.1 μm, probably due to an increase in the backbone surface area (Fig. 5b). Meanwhile, the optimal loading for the peak TPB length is increased with decreasing backbone particle size, indicating a sacrifice of electrode porosity. The percolated (active) TPB length shows a similar dependence on the infiltration loading with the total TPB length, as is shown in Fig. 5b. Two percolation thresholds are observed for $TPBL_{active}$ - the lower one and higher one corresponding to the percolation threshold of nanoparticles and pores, respectively. It is shown that the lower percolation threshold is quite close to the optimal infiltration loading for peak TPB length. Thus, the infiltration loading must be controlled carefully, especially for the electrode systems where TPB length is the performance limiting factor, e.g. LSM infiltrated YSZ electrodes.

As shown in Fig. 5c, the nanoparticles surface area shows a peak value at an infiltration loading of 35 vol.% (electrode porosity of 15 vol.%). Interestingly, the total nanoparticle surface area does not vary noticeably with varying backbone particle size. On the one hand, the initial backbone surface area is increased with decreasing backbone particle size (Fig. S1), providing more sites for nanoparticles infiltration. On the other hand, the amount of backbone particles is also increased. Thus the curved undercuts between backbone particles are much more easily flattened by the nanoparticles. Their combined effects may be the reason why the backbone particle size has little effect on nanoparticles surface area. In addition, the percolated surface area of nanoparticles, $AreaP_{NPS}$ (Fig. 5c) is almost the same as the total surface area, $Area_{NPS}$ between the low and high percolation thresholds. Based on the results shown in Fig. 5b and 5c, it is found that a variation in backbone particle size changes the TPB length but does not alter the nanoparticle surface areas. This finding offers an alternative way of identifying the electrode reaction mechanisms by measuring the cell performance with different backbone particle size. According to the model development, the summation of backbone surface area ($Area_{BBS}$) and the interface area of backbone-nanoparticles boundaries ($Area_{NBI}$) is equal to the initial backbone surface area. Therefore, both $Area_{BBS}$ and $Area_{NBI}$ are affected by the backbone particle size. As shown in Fig. S1, $Area_{NBI}$ ($Area_{BBS}$) increases (decreases) linearly with infiltration loading at the same rates for various backbone particle sizes, then approaches gradually to the initial backbone surface area (zero). The transitional point is the percolation threshold of $AreaP_{NBI}$ (Fig. S1), the same as that of nanoparticles, before which $Area_{NBI}$ is independent of backbone particle size. When the transition point is achieved, $AreaP_{NBI}$ tends to be stable (Fig. S1). Under normal infiltration loadings below 30 vol.%, all the backbone surface is percolated as shown in Fig. S1, because all the pores are percolated (Fig. 5a).

Effects of backbone porosity.— The backbone porosity is changed from 50 vol.% for the base case to 40 vol.% and 60 vol.% in this section. Fig. 6a shows the percolation probability of nanoparticles with

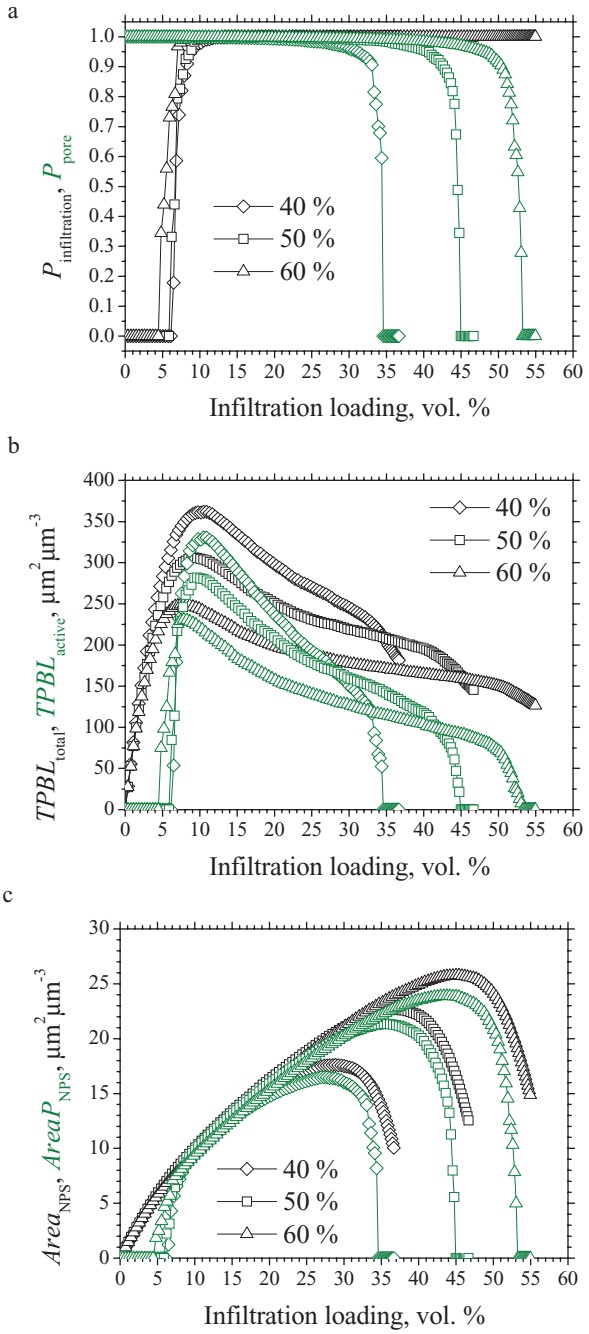

Figure 6. Calculation results of percolation probabilities of nanoparticles and pores (a), total and percolated TPB lengths (b), total and percolated nanoparticles surface areas (c) as a function of infiltration loading under various backbone porosities of 40 vol.%, 50 vol.%, and 60 vol.% ($r_{BB} = 0.2$ μm, $r_{NP} = 25$ nm, $w = 0.9$).

the three porosities. It is found that the percolation threshold only decreases slightly with increasing backbone porosity. Interestingly, this result is similar to the percolation theory for conventional composite electrodes, in which the percolation threshold is independent of electrode porosity.[19] Fig. 6a also presents the percolation probability of pores. It is found that the percolation threshold increases with the backbone porosity. However, it indicates a unique threshold of 10 vol.% in terms of electrode porosity, above which more than 95 percent of pores are percolated.

The total TPB length is shown in Fig. 6b. Similar to the effects of backbone particle size, a decrease in backbone porosity increases the peak TPB length, because decreasing backbone particle size and porosity increases the initial backbone surface area. Furthermore, the peak TPB length is proportional to the initial backbone surface area. For instance, the peak $TPBL_{total}$ for backbone porosities of 40 vol.%, 50 vol.%, and 60 vol.% is 370 $\mu m.\mu m^{-3}$, 300 $\mu m.\mu m^{-3}$, and 250 $\mu m.\mu m^{-3}$, respectively. And the corresponding initial backbone surface area is 8.1 $\mu m^2 \mu m^{-3}$, 6.8 $\mu m^2 \mu m^{-3}$, and 5.5 $\mu m^2 \mu m^{-3}$, respectively (Fig. S2). In fact, this rule is also applicable to the effects of backbone particle size. Despite of the backbone particle size and backbone porosity, $TPBL_{total}$ can be expressed as a function of (initial) backbone surface area, which will be presented in the following section. Note that the backbone surface area may be reduced for a smaller backbone porosity, say 30 vol.% which is, however, not usually used for infiltration. The percolated TPB length is also shown in Fig. 6b. As can be seen, once the percolation threshold is achieved, the peak percolated TPB length is obtained, thus the infiltration loading must be carefully controlled to achieve both good percolation properties and high TPB length.

Fig. 6c shows the dependence of nanoparticles surface area on backbone porosity. For the various backbone porosities, $Area_{NPS}$ is insensitive to backbone porosity at infiltration loading of below 20 vol.%. With an increase in backbone porosity, the peak $Area_{NPS}$ is enhanced and the corresponding infiltration loading is increased as well. The peak $Area_{NPS}$ corresponds to an electrode porosity of 15 vol.%. Similarly, the percolated nanoparticles surface area shown in Fig. 6c is independent of the backbone porosity at an infiltration loading of lower than 20 vol.%. Since the backbone porosity affects the TPB length but does not noticeably influence the nanoparticle surface area, varying the backbone porosity could be another method to identify electrode reaction mechanisms. One ideal model may be the samaria - doped ceria (SDC) infiltrated Ni anodes. Recently, Chueh and Haile studied well-defined SDC-Ni geometries and interfaces, and demonstrated that SDC nanoparticles surface area scales with electrode activity, rather than the TPB lines density.[27] Referring to the work by D. Ding et al.,[3] Fig. 7 shows the peak power densities of button cells supported by SDC infiltrated Ni anodes as a function of SDC loading. Three batches of button cells with anodic pore former loadings of 10 wt% (FC10), 20 wt% (FC20), and 30 wt% (FC30) are studied. It is shown that, before the maximum peak power density is reached, the power densities for the various backbone porosities are basically the same. But high backbone porosity leads to increase the peak power density. The tendency of nanoparticles surface area with infiltration loading (Fig. 6c) is in good agreement with this results,[3] validating the present study.

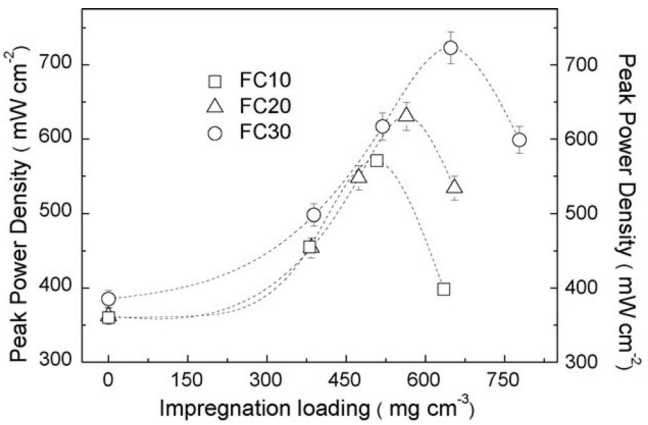

Figure 7. Reprint of the Fig. 6 in Ref. 3, showing the peak power densities (600°C) of SDC infiltrated Ni anode-based button cells under various SDC infiltration loading. FC10, 20, and 30 represent anodic pore former loading of 10 wt%, 20 wt%, and 30 wt%, respectively. (Reprinted with permission from Refs. 3. Copyright 2007 Elsevier.)

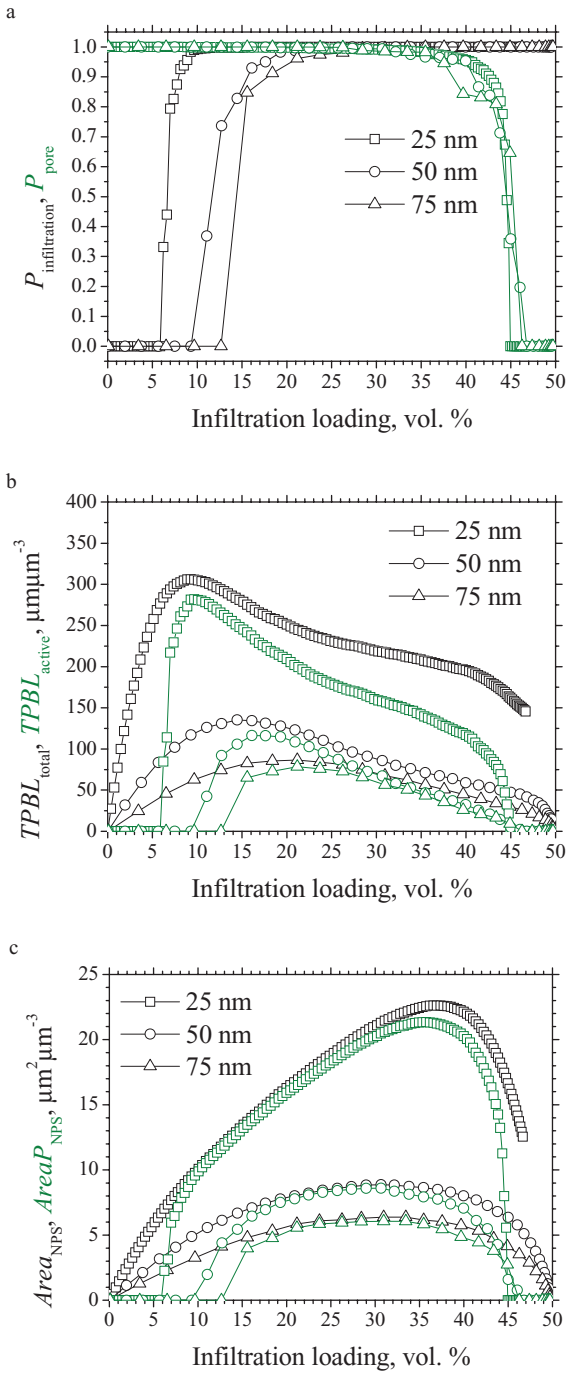

Figure 8. Calculation results of percolation probabilities of nanoparticles and pores (a), total and percolated TPB lengths (b), total and percolated nanoparticles surface areas (c) as a function of infiltration loading under various nanoparticle radiuses of 25 nm, 50 nm, and 75 nm (r_{BB} = 0.2 μm, backbone porosity = 50 vol.%, w = 0.9).

The backbone porosity affects the interface area of backbone-nanoparticles boundaries and the backbone surface area as well as their percolation properties in a similar way, shown in Fig. S2.

Effects of nanoparticle size.— Three groups of nanoparticle sizes with radiuses of 25 nm, 50 nm, and 75 nm are studied. Fig. 8a shows the percolation probability of nanoparticles. The percolation threshold is found to increase with increasing nanoparticle size, which is contrary with the effects of backbone particle size. Interestingly, the percolation probability of nanoparticles seems to be a function of the size ratio of nanoparticles to backbone particles, r_{NP}/r_{BB}. For example, the case r_{NP} = 25 nm, r_{BB} = 0.1 μm shown in Fig. 5a, and the case r_{NP} = 50 nm, r_{BB} = 0.2 μm shown in Fig. 8a have the same ratio, r_{NP}/r_{BB} = 0.25, and show a unique percolation threshold of 11 vol.%. The percolation threshold increases from 6 vol.% to 14 vol.% when the size ratio increases from 0.125 (Fig. 5a) to 0.375 (Fig. 8a). According to the percolation theory for conventional composite electrodes, the percolation threshold is only a function of particle size ratio.[19] However, for infiltrated electrodes, the percolation threshold of nanoparticles is not only a function of r_{NP}/r_{BB}, but also a function of aggregation risk of nanoparticles, which will be presented in the following section. The percolation of pores shows little dependence on the nanoparticle size (Fig. 8a).

As shown in Fig. 8b, the total TPB length ($TPBL_{total}$) can be remarkably enhanced by decreasing nanoparticle size. For example, a peak $TPBL_{total}$ length of 80 μm/μm^3 is shown in case of r_{NP} = 75 nm, while the peak TPB length is increased to 300 μm/μm^3 when the nanoparticle radius is reduced to 25 nm. Meanwhile, the optimal infiltration loading corresponding to the peak $TPBL_{total}$ is reduced from 20 vol.% to 10 vol.%. Accordingly, reducing nanoparticle size not only increases TPB length but also decreases the optimal infiltration loading, leading to a higher electrode porosity. As shown by the percolated TPB length in Fig. 8b, the optimal infiltration loading is approaching to the percolation threshold as reducing nanoparticle size.

Different from the effects of backbone structure, nanoparticles surface area is highly sensitive to the nanoparticle size. As shown in Fig. 8c, smaller nanoparticle size leads to higher total/percolated nanoparticles surface area. Thus reducing nanoparticle size essentially benefits electrode performance, because both the TPB length and nanoparticles surface area are enhanced. It should be mentioned that the nanoparticles surface area can be larger than the initial backbone surface area, depending on the nanoparticle size and infiltration loading. But in some cases, for instance r_{NP} = 75 nm shown in Fig. 8c, the nanoparticles surface area is always lower than the initial backbone surface area of 6.8 μm^2/μm^3, no matter what is the infiltration loading. This may be caused by the flattening of undercuts between backbone particles and the smoothing of nanoparticles surface. The other geometric parameters, including $Area_{NBI}$, $Area_{BBS}$, $AreaP_{NBI}$, and $AreaP_{BBS}$ are shown in Fig. S3. Their changing rates with infiltration loading are found to be increased by reducing nanoparticle size.

Effects of aggregation risk of nanoparticles.— As indicated by Eq. 1, the weighting parameter w represents the aggregation risk of nanoparticles. A higher w value indicates a lower risk to form nanoparticle aggregations. To reveal the effects of the aggregation risk, the w values are varied from 0.9 to 0.5 and 0.1. As shown in Fig. 9a, the percolation probability of nanoparticles decreases with increasing w. As expected, if the nanoparticles are uniformly coated onto backbone surface with a low risk of aggregation, a low infiltration loading is needed to form a continuous network of nanoparticles. In practice, the aggregation risk can be modified by tailoring the infiltration conditions. For example, Liang et al.[23] studied the Pd infiltrated YSZ electrodes by infiltration - chemical reduction process (Fig. 1c) and infiltration - thermal decomposition process (inset of Fig. 1c). As shown in Fig. 1c, the chemically reduced Pd nanoparticles tend to form aggregations, indicating poorly - percolated network, while the thermally decomposed Pd nanoparticles are coated uniformly onto the YSZ backbone surface, exhibiting lower electrode ASR.[23] In addition to the aggregation risk, the percolation threshold of nanoparticles is also a strong function of r_{NP}/r_{BB} as discussed above. Fig. 10a shows the contours of percolation threshold as a function of r_{NP}/r_{BB} and w, showing that the percolation threshold increases with increasing r_{NP}/r_{BB} and decreasing w. This can be verified by experimental observations. From the work by He et al.,[28] Fig. 10b shows the electric conductivity of LSM and (La,Sr)CoO_3 (LSC) infiltrates with infiltration loading. As shown, the percolation threshold of LSC infiltrate is ~10 vol.%, and the percolation threshold of LSM infiltrate is ~5 vol.%. As indicated by the inset SEM micrographs, compared with LSM infiltrate,

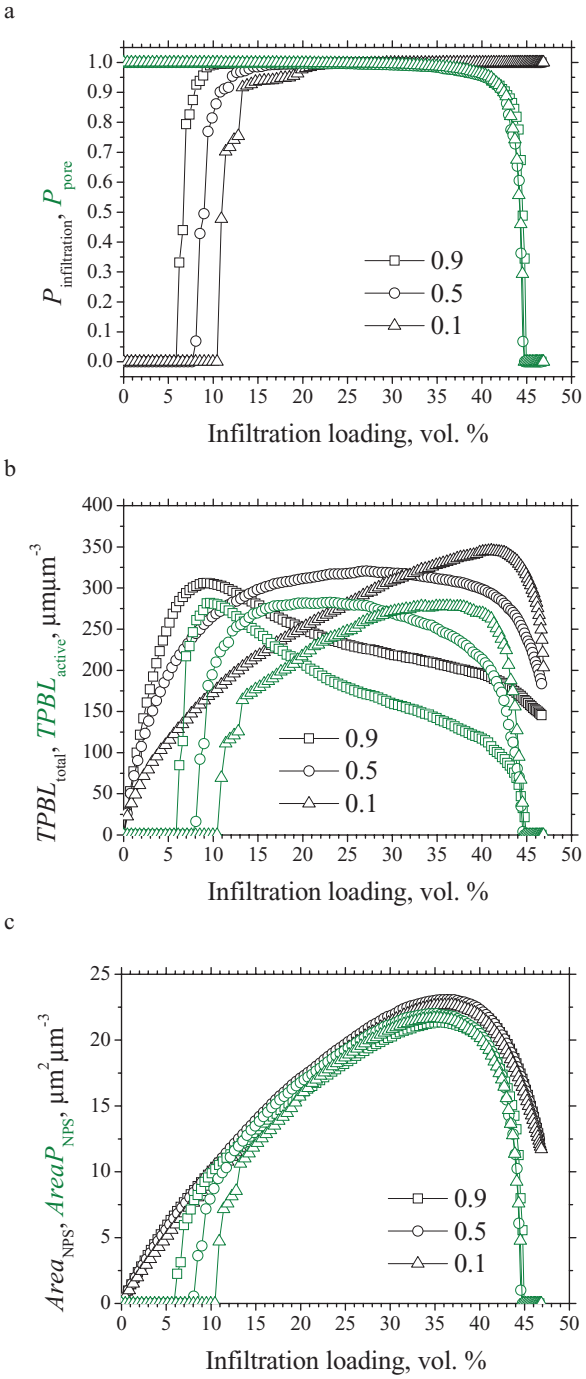

Figure 9. Calculation results of percolation probabilities of nanoparticles and pores (a), total and percolated TPB lengths (b), total and percolated nanoparticles surface areas (c) as a function of infiltration loading under various weighting parameters of 0.1, 0.5, and 0.9 (r_{BB} = 0.2 μm, backbone porosity = 50 vol.%, r_{NP} = 25 nm).

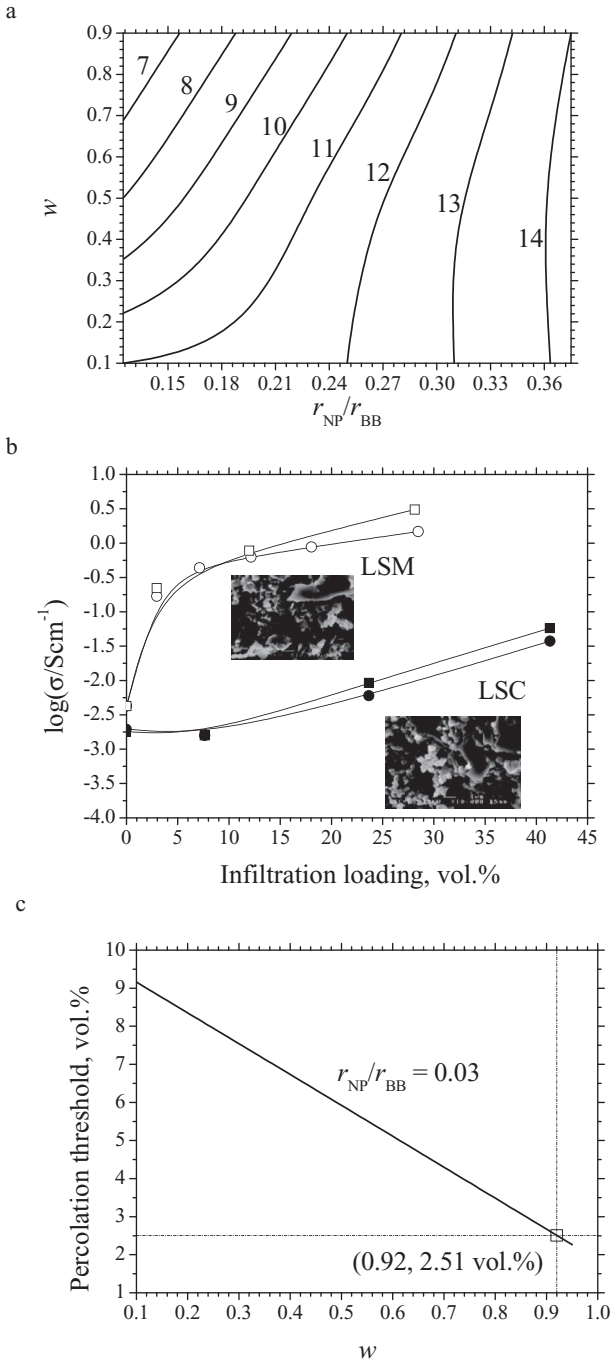

Figure 10. Contour plot of percolation threshold of infiltrated nanoparticles [vol.%] as a function of particle size ratio, r_{NP}/r_{BB} and weighting parameter, w (a). And the reported electric conductivities at 700°C for LSM infiltrated YSZ electrodes (open symbols) and LSC infiltrated YSZ electrodes (solid symbols) as a function of infiltration loading[28] (b). Square and circle symbols represents different infiltration conditions. The corresponding SEM micrographs are inset. And the illustration of w estimation based on the experimental data - r_{NP}/r_{BB} = 0.03, percolation threshold = 2.51 vol.% in[22] (c). (Scatters data and SEM micrographs in b are reprinted with permission from Refs. 28. Copyright 2004 The American Ceramic Society.)

LSC infiltrate has larger particle size and higher aggregation risk, hence higher percolation threshold. Zhan et al. reported that, all the nanoparticles are percolated at an infiltration loading of 2.51 vol.%, when r_{NP}/r_{BB} = 45 nm/1.5 μm for Ni infiltrated LSGM electrodes.[22] The corresponding weighting parameter, w could be estimated by using Fig. 10a. First, the contour plot data in Fig. 10a is extrapolated to obtain the percolation threshold vs. w relationship under r_{NP}/r_{BB} = 0.03 condition as shown in Fig. 10c. Then, w can be easily estimated as 0.92 for the reported percolation threshold of 2.51 vol.%. For high r_{NP}/r_{BB} values, the effects of w are not obvious. For example, in case of r_{NP}/r_{BB} = 0.15, the percolation threshold increases from 7 vol.% to 11 vol.% when w is decreased from 0.9 to 0.1. However, in case of r_{NP}/r_{BB} = 0.36, the percolation probability is about 14 vol.%, independent of w. At high r_{NP}/r_{BB} values, the infiltrated structure is similar to the morphology of conventional composite electrodes, in which the

percolation probability is only a function of particle size ratio. But there is essential difference between these two types of structures. For the conventional composite electrodes, particles are located randomly in the 3D space. While for the infiltrated electrodes, the nanoparticles are coated onto the backbone surface, which is a highly curved surface with a fractional dimension between 2D and 3D. Fig. 9a also shows the percolation probability of pores, indicating no dependence on w. In summary, the percolation probability of pores is only a function of electrode porosity.

The total and percolated TPB length is shown in Fig. 9b. It is found that the peak TPB length only increase slightly, while the optimal infiltration loading increases significantly with decreasing weighting parameter (w). For instance, the optimal loading increases from 10 vol.% to 25 vol.% when w decreases from 0.9 to 0.5. That means lower infiltration loading is sufficient to enhance TPB length, if the nanoparticles can be coated uniformly onto backbone surface.

As shown in Fig. 9c, the weighting parameter has negligible effect on the nanoparticles surface area, probably because the roughness of nanoparticle surface is not affected by the weighting parameter. Due to the increase of aggregation risk (decrease of w), $Area_{\mathrm{NBI}}$, $Area_{\mathrm{BBS}}$, $AreaP_{\mathrm{NBI}}$, and $AreaP_{\mathrm{BBS}}$ evolves much gradually with increasing infiltration loading, shown in Fig. S4.

Analytical model – $Area_{BBS}$ and $Area_{NPS}$ vs. infiltration loading.— It can be seen from the above discussions that the infiltration loading, t [vol.%] is an important parameter affecting the nanoparticles surface area ($Area_{\mathrm{NPS}}$) and the backbone surface area ($Area_{\mathrm{BBS}}$). During the numerical infiltration, the backbone surface area is reduced as part of it is covered by nanoparticles. When the infiltration loading is increased by a small step of dt, the backbone surface area is decreased by $dArea_{\mathrm{BBS}}$. It is noted that only an infiltration loading of $P_{\mathrm{BBS}}dt$ is coated on the backbone surface, where P_{BBS} is the probability for nanoparticles coated onto the backbone surface (refer to Eq. 1). Furthermore, the decrease of backbone surface area, $dArea_{\mathrm{BBS}}$ can be related to the effective infiltration loading, $P_{\mathrm{BBS}}dt$, as,

$$dArea_{\mathrm{BBS}} = -k_0 P_{\mathrm{BBS}} dt \qquad [2a]$$

where k_0 [$\mu m^2 \mu m^{-3}$/vol.%] represents the area reduction of backbone surface for nanoparticles per unit infiltration loading on the backbone surface. In addition, k_0 is constant below infiltration of 30 vol.%, which will be discussed later. On the other hand, the nanoparticles surface area is increased by $dArea_{\mathrm{NPS}}$, derived from nanoparticles coated onto the backbone surface and nanoparticles coated onto the nanoparticles surface,

$$dArea_{\mathrm{NPS}} = k_1 P_{\mathrm{BBS}} dt + k_2 (1 - P_{\mathrm{BBS}}) dt \qquad [2b]$$

where k_1 [$\mu m^2 \mu m^{-3}$/vol.%] represents the area increase of nanoparticles surface for nanoparticles per infiltration loading coated onto the backbone surface, and k_2 [$\mu m^2 \mu m^{-3}$/vol.%] represents the increase in nanoparticle surface area for nanoparticles per infiltration loading coated onto nanoparticle surface. k_1 and k_2 are also assumed to be constant below infiltration loading of 30 vol.%. Inserting Eq. 1 into Eq. 2, and solving the differential equations with an initial backbone surface area, $Area^0_{\mathrm{BBS}}$ gives two groups of solutions depending on k_2. If $k_2 \neq 0$, it gives,

$$t = -\left\{\frac{1}{k_0} - \frac{(1-w)k_1}{k_0[(1-w)k_2 + wk_0]}\right\} Area_{\mathrm{BBS}} - \frac{k_1 - k_2}{k_0 k_2} Area^0_{\mathrm{BBS}} + \left\{\frac{k_1 - k_2}{k_0 k_2} + \frac{1}{k_0} - \frac{(1-w)k_1}{k_0[(1-w)k_2 + wk_0]}\right\} \times Area^0_{\mathrm{BBS}} \left(\frac{Area^0_{\mathrm{BBS}}}{Area_{\mathrm{BBS}}}\right)^{\frac{(1-w)k_2}{wk_0}} \qquad [3a]$$

and

$$(k_1 - k_2) Area_{\mathrm{BBS}} + k_0 Area_{\mathrm{NPS}} = k_0 k_2 t + (k_1 - k_2) Area^0_{\mathrm{BBS}} \qquad [3b]$$

If $k_2 = 0$, it gives,

$$t = \frac{wk_0 - (1-w)k_1}{wk_0^2}\left(Area^0_{\mathrm{BBS}} - Area_{\mathrm{BBS}}\right) + \frac{(1-w)k_1}{wk_0^2} Area^0_{\mathrm{BBS}} \ln \frac{Area^0_{\mathrm{BBS}}}{Area_{\mathrm{BBS}}} \qquad [4a]$$

and

$$k_1 Area_{\mathrm{BBS}} + k_0 Area_{\mathrm{NPS}} = k_1 Area^0_{\mathrm{BBS}} \qquad [4b]$$

By using Eq. 3 and Eq. 4, $Area_{\mathrm{BBS}}$ and $Area_{\mathrm{NPS}}$ can be calculated at an given infiltration loading, t. Meanwhile, $Area_{\mathrm{NBI}}$ can be also calculated as $Area^0_{\mathrm{BBS}}$ - $Area_{\mathrm{BBS}}$. It is believed that k_0, k_1, and k_2 are related to the backbone structure, and nanoparticle size, but the quantitative relationships are not clear yet. Instead, they are used as fitting parameters. Eq. 3 and Eq. 4 are fitted to the data of numerical infiltration, and then a better fitting result is selected by using the criterion of fitting goodness (R-square). For validation, the SR model is used, in which the surface area of nanoparticles is estimated as the surface area summation of hemispherical nanoparticles, $Area_{\mathrm{NPS}} = 3t/r_{\mathrm{NP}}$.[4] Fig. 11 shows the validation results for various conditions, including the effects of backbone particle size (Fig. 11a), backbone porosity (Fig. 11b), nanoparticle size (Fig. 11c), and weighting parameter (Fig. 11d). It is shown that the linear relationship (dashed lines), $Area_{\mathrm{NPS}} = 3t/r_{\mathrm{NP}}$ agrees well with the numerical infiltration results at low infiltration loading, e.g. less than 7 vol.%, under which the nanoparticles may be isolated between each other. However, the discrepancy occurs and increases with increasing infiltration loading due to the contacting between nanoparticles (Fig. 1d and Fig. 4c). Eq. 3 and 4 fit well with the numerical infiltration data under the various conditions. The fitted values for k_0, k_1, and k_2 are listed in Table I. It is found that, Eq. 4 is more suitable for high $r_{\mathrm{NP}}/r_{\mathrm{BB}}$ and low w conditions, suggesting that the nanoparticles coated onto the nanoparticles surface do not contribute to the nanoparticles surface area for high $r_{\mathrm{NP}}/r_{\mathrm{BB}}$ and low w levels.

The fitting and numerical construction results can be further validated by comparing the calculated electrode ASR with data from the literature. According to the SR model, ASR of mixed ionic - electronic conductor (MIEC) infiltrated electrode can be given by,

$$ASR = R_s/\lambda Area_{\mathrm{NPS}} \qquad [5]$$

where R_s is the fundamental ASR of MIEC infiltrate (Ωcm^2), λ is the electrode thickness (μm). As discussed above, the nanoparticles surface area, $Area_{\mathrm{NPS}}$ is only affected by nanoparticle size and infiltration loading. The nanoparticle radius for the baseline is 25 nm, the same as the experimental work for LSCF infiltrated GDC electrode by Shah et al.[4] Thus the fitting results of $Area_{\mathrm{NPS}}$ by Eq. 3 for the baseline condition were inserted into Eq. 5. Note that Eq. 5 neglects the resistance of backbone structure, while the recently proposed SIMPLE model by Nicholas et al. considered it.[13] Thus the SIMPLE model is also used for validation. The reported parameters from the literature are used for model validation. For example, R_s of LSCF is 100 Ωcm^2 at 600°C and 10 Ωcm^2 at 700°C (for use of SR model and SIMPLE model); Ionic conductivity of GDC is 0.0117 Scm^{-1} at 600°C and 0.0272 Scm^{-1} at 700°C (for use of SIMPLE model).[4] The comparison between the reported experimental data (symbols) and the calculation results (lines) are shown in Fig. 12. As is shown, the calculated results basically agree with the experimental data. The discrepancy between the SR model and the SIMPLE model derives from the resistance of GDC backbone. In other words, the constructed results of the baseline could be used to represent the experimental microstructure of LSCF infiltrated GDC electrode. The SIMPLE model and the model developed in the present paper could serve as useful tools for predicting the actual infiltrated electrode performance.

Analytical model – $TPBL_{total}$ vs. $Area_{BBS}$ and r_{NP}.— In principle, the TPB length per unit volume ($TPBL_{\mathrm{total}}$) can be estimated if the initial backbone surface area per volume ($Area^0_{\mathrm{BBS}}$) and TPB length per initial backbone surface area are known. As illustrated in Fig. 2,

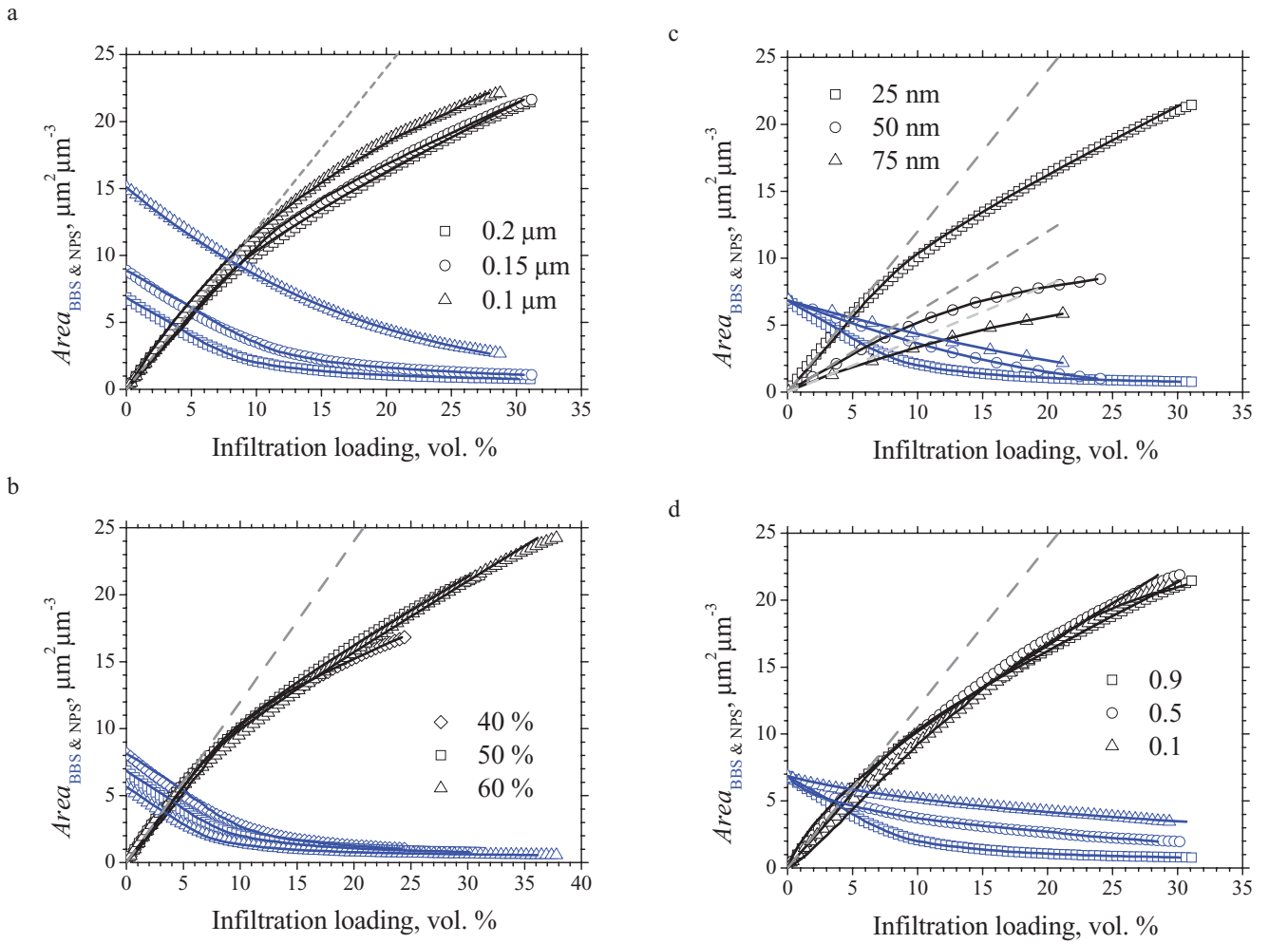

Figure 11. Validation of Eq. 3 or 4 (solid lines) by the numerical infiltration results (scatter plots) under various conditions, including the effects of backbone particle size (a), backbone porosity (b), infiltrated particle size (c) and weighting parameter (d). For comparison, the model by Shah et al.[4] is shown in dashed lines.

the radius of the contact ring at a backbone-nanoparticle contact can be considered as the nanoparticle radius, r_{NP}. Let the contact numbers of nanoparticles per unit initial backbone surface area be n [μm^{-2}], we can estimate the circumference summation of contact rings per unit initial backbone surface area as $n(2\pi r_{NP})$. However, this cannot be used as the estimation of TPB length per initial backbone surface area, due to possible overlapping between these contact rings (Fig. 1d). Only these segments of contact rings contacting with pores form TPBs. Similar with the model by Gokhale et al.,[29] the TPB length per initial backbone surface area may be estimated as the circumference summation $n(2\pi r_{NP})$ weighted by the area fraction of remaining backbone surface, $Area_{BBS}/Area^0_{BBS}$. Thus the TPB length per volume is given by,

$$TPBL_{total} = Area^0_{BBS} n(2\pi r_{NP}) Area_{BBS}/Area^0_{BBS} \quad [6a]$$

On the other hand, the area summation of contact rings per volume is,

$$Area^{ext}_{NBI} = Area^0_{BBS} n\pi r^2_{NP} \quad [6b]$$

The superscript 'ext' indicates the 'extended' interface area of backbone-nanoparticles boundaries, including the overlapped areas of contact rings. According to the Johnson – Mehl - Avrami theory,[30] which is usually used in nucleation, the extended interface area, $Area^{ext}_{NBI}$ is linked to the real interface area $Area_{NBI}$ as,

$$\frac{Area_{NBI}}{Area^0_{BBS}} = 1 - \exp\left(-\frac{Area^{ext}_{NBI}}{Area^0_{BBS}}\right) \quad [6c]$$

This may be ideal because the formation of infiltrated nanoparticles is also a nucleation process. But it should be noted that the minimal distance between infiltrated nanoparticles is limited by the contact

Table I. Fitting values of $k_{0,\ 1\ and\ 2}$ at various conditions.

		r_{BB}, μm		r_{NP}, nm		Porosity, vol.%		w	
	Baseline	0.1	0.15	50	75	40	60	0.5	0.1
k_0	0.3805	0.8097	0.4381	0.3666	0.2726	0.4820	0.3057	0.6102	0.2585
k_1	0.9131	5.4299	0.9334	1.3021	0.8462	0.9393	0.8540	1.5246	0.0987
k_2	0.4814	0	0.3935	0	0	0.3129	0.5135	0.4707	0

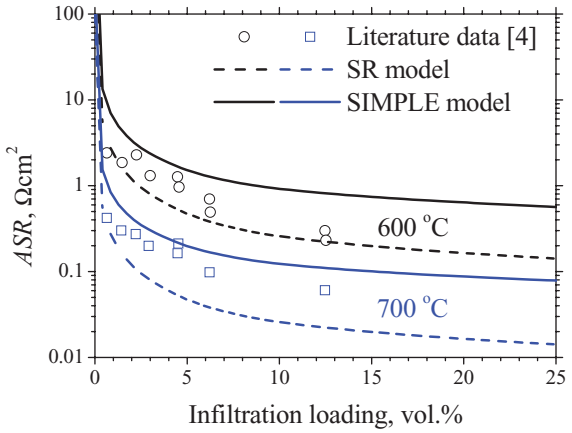

Figure 12. Model validation by using the reported ASR of LSCF infiltrated GDC electrode,[4] SR model, and SIMPLE model. (Scatters data is reprinted with permission from Refs. 4. Copyright 2008 Elsevier.)

angle due to the sintering process. This is a little different from the nucleation process, in which the nucleation sites are not restricted by distance. Thus we introduce a dimensionless scaling factor, κ into Eq. 6c,

$$\frac{Area_{\mathrm{NBI}}}{Area^{0}_{\mathrm{BBS}}} = 1 - \exp\left(-\kappa \frac{Area^{\mathrm{ext}}_{\mathrm{NBI}}}{Area^{0}_{\mathrm{BBS}}}\right) \qquad [6d]$$

Eq. 6d is validated by the numerical construction results when κ is equal to 2/3. Combining Eq. 6b and 6d, the contact numbers of nanoparticles per initial backbone surface area is given by,

$$n = \frac{3}{2\pi r^{2}_{\mathrm{NP}}} \ln \frac{Area^{0}_{\mathrm{BBS}}}{Area_{\mathrm{BBS}}} \qquad [6e]$$

Inserting Eq. 6e into Eq. 6a, the TPB length per volume is obtained,

$$TPBL_{\mathrm{total}} = \frac{3Area_{\mathrm{BBS}}}{r_{\mathrm{NP}}} \ln \frac{Area^{0}_{\mathrm{BBS}}}{Area_{\mathrm{BBS}}} \qquad [7]$$

which is free from fitting parameters.

Fig. 13 shows the plots of Eq. 7 and the corresponding scatter plots of numerical infiltration data, showing Eq. 7 agrees nicely with the numerical construction results under the various conditions. The backbone surface area corresponding to the peak TPB length yields,

$$dTPBL_{\mathrm{total}}/dArea_{\mathrm{BBS}} = 0 \qquad [7a]$$

By solving Eq. 7a, it gives,

$$Area_{\mathrm{BBS}}/Area^{0}_{\mathrm{BBS}} = 1/e \qquad [7b]$$

It means that the maximum TPB length is achieved at 63% coverage of backbone surface by nanoparticles. And the peak TPB length is governed by the initial backbone surface area and the radius of infiltrated nanoparticles, given by 1.11 $Area^{0}_{\mathrm{BBS}}/r_{\mathrm{NP}}$.

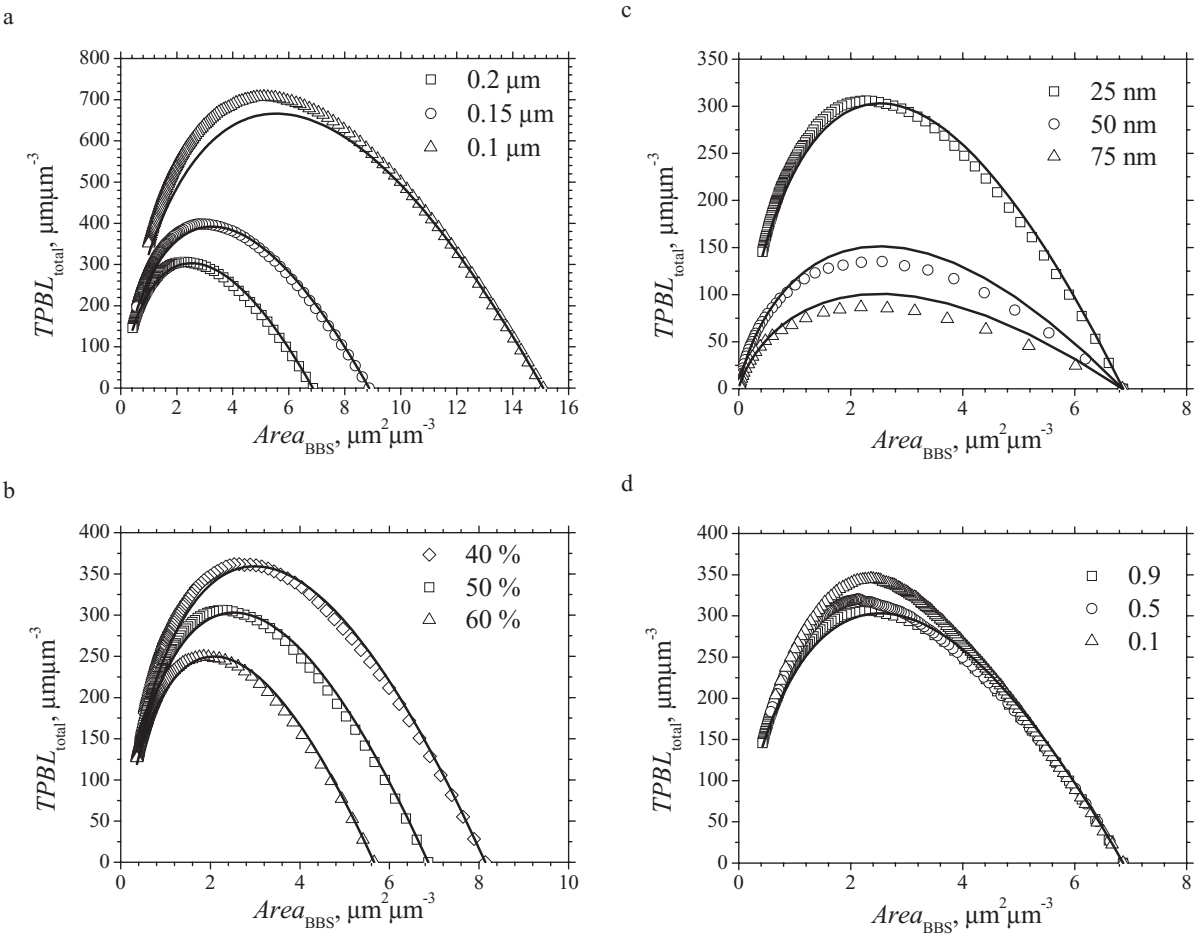

Figure 13. Validation of Eq. 6 (solid lines) by the numerical infiltration results (scatter plots) under various conditions, including the effects of backbone particle size (a), backbone porosity (b), infiltrated particle size (c) and weighting parameter (d).

Table II. The marking of factors that affect geometric properties. Blank space means little or no effect.

	$P_{infiltration}$	P_{pore}	$TPBL_{total}$	$TPBL_{active}$	$Area_{NPS}$	$AreaP_{NPS}$	$Area_{NBI}$	$AreaP_{NBI}$	$Area_{BBS}$	$AreaP_{BBS}$
Infiltration loading	√	√	√	√	√	√	√	√	√	√
r_{BB}	√		√	√			√	√	√	√
Backbone porosity		√	√	√			√	√	√	√
r_{NP}	√		√	√	√	√	√	√	√	√
w	√		√	√			√	√	√	√

Conclusion

By using the numerical infiltration method, important microstructure properties are calculated as a function of infiltration loadings, including the percolation probabilities of infiltrated nanoparticles and pores, total and percolated properties of TPB length, nanoparticles surface area, backbone surface area, and interface area of backbone-nanoparticles boundaries. The effects of backbone particle size, backbone porosity, infiltrated nanoparticle size, and the aggregation risk of nanoparticles on various microstructure properties and percolation properties are studied in detail. Table II summarizes the factors that can affect these geometrical properties. The parametric study leads to the following interesting conclusions:

(1) The percolation threshold of infiltrated nanoparticles depends on the ratio of nanoparticle size to the backbone particle size (r_{NP}/r_{BB}), and the weighting parameter, w, which represents the aggregation risk of nanoparticles. The threshold infiltration loading is much lower than that for conventional composite electrodes.
(2) The percolation threshold of pores is only a function of electrode porosity. At an electrode porosity of higher than 10 vol.%, more than 95% pores are interconnected for gas diffusion.
(3) Backbone particle size and backbone porosity have little effect on nanoparticles surface area, but exhibit remarkable effects on TPB length. Thus modifying backbone structure can be an effective strategy to identify electrode reaction mechanisms, i.e. whether the reaction occur at TPB or on the surface.
(4) Decreasing the size of the nanoparticles remarkably enhances the TPB length and increases the nanoparticle surface area. In addition, with smaller nanoparticle size, the optimal infiltration loading corresponding to the peak TPB length is decreased, leading to a higher electrode porosity. Thus decreasing infiltrated particle size essentially benefits electrode performance.

Analytical models are developed to establish relationship between the infiltration loading and the surface areas of nanoparticles/backbone as well as the relationship among the TPB length, backbone surface area and infiltrated particle size. Both models agree well with the numerical infiltration results. Particularly, the analytical model for TPB length is free from fitting parameters and can be used as a useful tool for fast estimation of the infiltrated electrode properties. It is found that the peak TPB length can be achieved when 63% of the backbone surface is coated by infiltrated particles.

Acknowledgment

This research was supported by a grant (Project Number: PolyU 5238/11E) from Research grant Council (RGC) of Hong Kong, the financial support of the Ministry of Science and Technology of China (2012CB215403) and the Ministry of Education of China (20113402110014).

References

1. S. P. Jiang, *Int. J. Hydrogen Energy*, **37**, 449 (2012).
2. W Zhu, D. Ding, and C. R. Xia, *Electrochem. Solid-State Lett.*, **11**, B83 (2008).
3. D Ding, W. Zhu, J. F. Gao, and C. R. Xia, *J. Power Sources*, **179**, 177 (2008).
4. M. Shah, J. D. Nicholas, and S. A. Barnett, *Electrochem. Commun.*, **11**, 2 (2009).
5. J. D. Nicholas and S. A. Barnett, *J. Electrochem. Soc.*, **156**, B458 (2009).
6. S. P. Jiang, *Mater. Sci. Eng. A*, **418**, 199 (2006).
7. J. M. Vohs and R. J. Gorte, *Adv. Mater.*, **21**, 943 (2009).
8. S. B. Adler, *Chem. Rev.*, **104**, 4791 (2004).
9. R. Radhakrishnan, A. V. Virkar, and S. C. Singhal, *J. Electrochem. Soc.*, **152**, A210 (2005).
10. Y Zhang and C. R. Xia, *J. Power Sources*, **195**, 4206 (2010).
11. R. Kungas, F. Bidrawn, E. Mahmoud, J. M. Vohs, and R. J. Gorte, *Solid State Ionics*, **225**, 146 (2012).
12. C. W. Tanner, K. Fung, and A. V. Virkar, *J. Electrochem. Soc.*, **144**, 21 (1997).
13. J. D. Nicholas, L. Wang, A. V. Call, and S. A. Barnett, *Phys. Chem. Chem. Phys.*, **14**, 15379 (2012).
14. J. R. Wilson, W. Kobsiriphat, R. Mendoza, H. Y. Chen, J. M. Hiller, D. J. Miller, K. Thornton, P. W. Voorhees, S. B. Adler, and S. A. Barnett, *Nat. Mater.*, **5**, 541 (2006).
15. A. Tkachuk, F. Duewer, H. Cui, M. Feser, S. Wang, and W. Yun, *Z. Kristallogr.*, **222**, 650 (2007).
16. J. Golbert, C. S. Adjiman, and N. P. Brandon, *Ind. Eng. Chem. Res.*, **47**, 7693 (2008).
17. B. Kenney, M. Valdmanis, C. Baker, J. G. Pharoah, and K. Karan, *J. Power Sources*, **189**, 1051 (2009).
18. Y Zhang, C. R. Xia, and M. Ni, *Int. J. Hydrogen Energy*, **37**, 3392 (2012).
19. P. Costamagna, P. Costa, and V. Antonucci, *Electrochim. Acta*, **43**, 375 (1998).
20. Q. Cai, C. S. Adjiman, and N. P. Brandon, *Electrochim. Acta*, **56**, 5804 (2011).
21. F. Liang, J. Chen, S. P. Jiang, B. Chi, J. Pu, and L. Jian, *Electrochem. Commun.*, **11**, 1048 (2009).
22. Z. L. Zhan, D. M. Bierschenk, J. S. Cronin, and S. A. Barnett, *Energ. Environ. Sci.*, **4**, 3951 (2011).
23. F. Liang, W. Zhou, B. Chi, J. Pu, S. P. Jiang, and L. Jian, *Int. J. Hydrogen Energy*, **36**, 7670 (2011).
24. R. M. Haralick, R. M. Shapiro, and G Linda, *Computer and Robot Vision*, Addison-Wesley, New York (1992).
25. J. R. Wilson, J. S. Cronin, A. T. Duong, S. Rukes, H. Y. Chen, K. Thornton, D. R. Munn, and S. A. Barnett, *J. Power Sources*, **195**, 1829 (2010).
26. H. He, Y. Huang, J. Regal, M. Boaro, J. M. Vohs, and R. J. Gort, *J. Am. Ceram. Soc.*, **87**, 331 (2004).
27. W. C. Chueh, Y. Hao, W. Jung, and S. M. Haile, *Nat. Mater.*, **11**, 155 (2012).
28. H. He, Y. Huang, J. Regal, M. Boaro, J. M. Vohs, and R. J. Gorte, *J. Am. Ceram. Soc.*, **87**, 331 (2004).
29. A. M. Gokhale, S. Zhang, and M. L. Liu, *J. Power Sources*, **194**, 303 (2009).
30. W. B. Robert, S. M. Allen, and W. C. Carter, *Kinetics of Materials*, Hoboken, New Jersey (2005).